Core Shell Inversion during Nucleation and Growth of Bimetallic Pt/Ru Nanoparticles

6 AUTHORS, INCLUDING:

John R Shapley
University of Illinois, Urbana-Champaign
252 PUBLICATIONS **5,832** CITATIONS

Core Shell Inversion during Nucleation and Growth of Bimetallic Pt/Ru Nanoparticles

Michael S. Nashner, Anatoly I. Frenkel, David Somerville, Charles W. Hills, John R. Shapley,* and Ralph G. Nuzzo*

Contribution from the School of Chemical Sciences and the Frederick Seitz Materials Research Laboratory, University of Illinois, Urbana, Illinois 61801

Received February 25, 1998

Abstract: The reductive condensation of a carbon-supported molecular cluster precursor, $PtRu_5C(CO)_{16}$, into a bimetallic nanoparticle has been followed by using in situ extended X-ray absorption fine structure spectroscopy, temperature-programmed desorption, and scanning transmission electron microscopy. The data reveal that during activation in hydrogen the metal centers associated with the molecular precursor lose the stabilizing CO shell and assume an increasingly metallic electronic character. This support-mediated condensation process is highly activated. The incipient Pt−Ru nanoparticles initially form a disordered structure at 473 K in which Pt is found preferentially at the core of the condensing particle. After further high-temperature treatment to 673 K, the nanoparticles adopt an inverted structure in which Pt appears preferentially at the surface of the equilibrated bimetallic nanoparticle.

Introduction

The chemically activated nucleation and growth of nanoscale compound and alloy materials is of fundamental importance in such areas as heterogeneous catalysis, microelectronics, and advanced materials synthesis.[1−5] The rational design of nanoscale structures for applications in technology increasingly relies on developing an improved understanding of these dynamical processes, particularly in terms of how they contribute to the phase behavior of nanoscale systems. The limited understanding of these processes obtained to date reflects, in large part, the inherent difficulty of preparing and characterizing well-defined nanometer-sized alloy and intermetallic phases for fundamental structural studies. Furthermore, the methods available to characterize the phase dynamics of nanoscale systems are limited.

One particularly valuable method for probing nanocluster structure is X-ray absorption spectroscopy. Several representative examples demonstrate the types of information which can be obtained about nanoscale materials using this technique. Extended X-ray absorption fine structure (EXAFS) has been used to study CdSe nanoparticles and to distinguish between bulk and surface structural behavior.[5−8] In these cases, the first coordination shell around the central atoms was analyzed by using either experimental[6,7] or theoretical[8] standards. Both

EXAFS and X-ray absorption near-edge structure (XANES) techniques were combined to determine interatomic distances, coordination numbers, local disorder, and the effective valence around Mn impurity ions in ZnS:Mn nanocrystals.[9] The size-dependent structural evolution of free Ar clusters has been analyzed recently by EXAFS by applying a multiple-scattering formalism.[10] The results suggest that the evolution of Ar clusters appears to occur through a transition from an icosahedral structure to that of a face-centered cubic structure as the cluster size increases. Our recent work has shown how EXAFS methods can be used to determine the structure of and demonstrate selective surface segregation in carbon-supported Pt−Ru nanoparticles. These close-packed structures were analyzed through the fourth coordination shell around both Pt and Ru centers by taking into account multiple-scattering contributions to the EXAFS.[11]

In the present study, we examine the nucleation and growth of a nearly homogeneous population of carbon-supported bimetallic nanoclusters. We have shown previously that heterometallic molecular carbonyl clusters can be used to prepare nanoscale supported bimetallic particles with narrow size and compositional distributions.[11] The uniform microstructural distribution obtained using this preparative method is, in large part, a consequence of the ability of the molecular precursor to mediate the transport-dependent nucleation and growth of nanometer-sized alloy particles. This study develops insights into the nature of these nucleation and growth processes for a representative binary metal alloy nanocrystalline solid. We show in this study, via a detailed in situ characterization of the microstructural evolution using X-ray absorption spectroscopy and scanning transmission electron microscopy, that the acti-

(1) *Clusters and Colloids*; Schmid, G., Ed.; VCH: Weinheim, 1994.

(2) Toles, W. M. In *Nanotechnology: Molecularly Designed Materials*; Chow, G., Gonsalves, K. E., Eds.; ACS Symposium Series 622; American Chemical Society: Washington, DC, 1995; pp 1−18.

(3) Schwartz, J. A. In *Surface Segregation Phenomena*; Dowben, P. A.; Miller, A., Eds.; CRC Press: Boca Raton, FL, 1990; Chapter 12.

(4) (a) Davis, R. J.; Boudart, M. *J. Phys. Chem.* **1994**, *98*, 5471. (b) Via, G. H.; Drake, K. F., Jr.; Meitzner, G.; Lytle, F. W.; Sinfelt, J. H. *Catal. Lett.* **1990**, *5*, 234. (c) Rodriquez, A.; et al. *Chem. Mater.* **1996**, *8*, 1978. (d) Nashner, M. S.; et al. *J. Am. Chem. Soc.* 1996, *118*, 12964.

(5) Andrews, M. P.; Ozin, G. A. *Chem. Mater.* **1989**, *1*, 174.

(6) Marcus, M. A.; Flood, W.; Steigerwald, W.; Brus, L.; Bawendi, M. *J. Phys. Chem.* **1991**, *95*, 372.

(7) Marcus, M. A.; Brus, L. E.; Murray, C.; Bawendi, M. G. *J. Am. Chem. Soc.* **1993**, *115*, 8706.

(8) Carter, A. C.; Bouldin, C. E.; Kemner, K. M.; Bell, M. I.; Woicik, C.; Majetich, S. A. *Phys. Rev. B* **1997**, *55*, 13822.

(9) Soo, Y. L.; Ming, Z. H.; Huang, S. W.; Kao, Y. H.; Bhargava, R. N.; Gallagher, D. *Phys. Rev. B* **1994**, *50*, 7602.

(10) Kakar, S.; Bjorneholm, O.; Weigelt, J.; de Castro, A. R. B.; Troger, L.; Frahm, R.; Moller, T.; Knop, A.; Ruhl, E. *Phys. Rev. Lett.* **1997**, *78*, 1675.

(11) Nashner, M. S.; Frenkel, A. I.; Adler, D. L.; Shapley, J. R.; Nuzzo, R. G. *J. Am. Chem. Soc.* **1997**, *119*, 7760.

Scheme 1
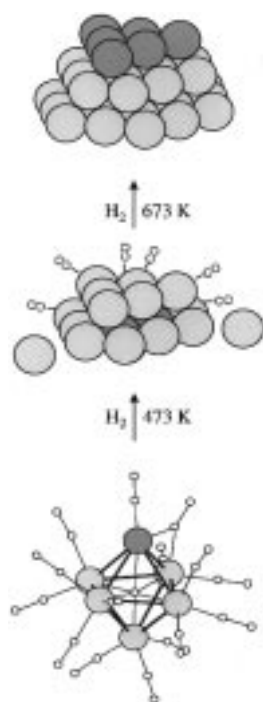
vated nucleation of these phases proceeds via the formation of a nascent homometallic core.

Specifically, we describe the processes involved in the nucleation and growth of catalytically active nanoscale Pt−Ru particles derived from a carbon-supported PtRu$_5$C(CO)$_{16}$ molecular cluster precursor. The structural evolution seen during the condensation of the nanoparticles involves the initial nucleation of a compact (Pt-rich) structure followed by the inversion of the intraparticle distribution of the Pt and Ru atoms upon continued high-temperature annealing. In this inversion, the core-segregated Pt atoms exchange with Ru surface atoms to form a surface Pt shell structure. During the entire evolution process, the bonds between the surface atoms and CO ligands gradually break; these kinetics appear to control the rate of formation of the final metallic state of the nanocluster. A qualitative model of the nucleation and growth processes characterized in this study is presented in Scheme 1. We believe that the dynamic structural transformation revealed in this work is in large part a result of the strong influence that the finite size of the assembly imparts on the kinetics and overall energetics. In the nanoparticles prepared here, over 50% of the metals occupy surface (i.e., low coordination) sites. This bonding environment strongly directs a nonstatistical partitioning of the metal species present in the nanoparticle. Of paramount interest is the demonstration made in this work of the progressions of reconstructions that can occur during the nucleation and growth of nanoscopic metal crystals.

Experimental Section

Sample Preparation. The molecular cluster precursor, PtRu$_5$C-(CO)$_{16}$, was prepared by methods described in the literature.[12] Suitable quantities of the compound (1−2 wt % metal loading) were dispersed on carbon black (Vulcan XC-72, Cabot) by incipient wetness from a THF solution. The mixture was allowed to dry in air for 1 h.

Temperature-Programmed Decomposition. The decomposition of the supported cluster precursor was monitored on a catalyst line that included a gas handling system, catalytic reactor, and equipment

for analysis of the effluent.[13] Prior to activation, each sample was evacuated for 1 h to remove residual solvent adsorbed on the carbon. A stream of H$_2$ (Matheson, 99.95%) was deoxygenated over Cr(II)/SiO$_2$ and dried over activated molecular sieves. The Pyrex U-tube reactor contained a course frit supporting the catalyst bed, which was in contact with a thermocouple well containing an Omega type-K Chromel/Alumel thermocouple. The reactor was heated by a tube furnace controlled with an Omega CN2011 temperature controller. In these experiments, the samples were activated by heating (with a linear temperature ramp, 15 K/min) to 773 K under a stream of H$_2$ (40 mL/min) and holding at that limit for 1 h. The effluent was monitored by a computer-interfaced Dyco quadrupole mass spectrometer (model M100M), which was connected immediately downstream from the reactor by a silica capillary.

Scanning Transmission Electron Microscopy (STEM). Microscopy studies were performed using a field emission Vacuum Generators HB501 STEM operated at 100 kV. The resolution of the microscope is estimated to be ∼3 Å. The specimens were prepared by dipping a copper-mesh-supported holey carbon grid (SPI Supplies) into powdered samples that had been previously activated and examined in situ by EXAFS. Image analysis was performed with Digital-micrograph (Gatan) digital-video data-acquisition software. The particle sizes were determined by measuring the cross-sectional intensity profiles of individual nanoparticles. The particle diameter was measured as the full width at half-maximum (fwhm) of the intensity profile.

In Situ X-ray Absorption Fine Structure. EXAFS data were collected as described in an earlier report.[11] Briefly, in situ X-ray absorption data were collected from a pellet sample formed by pressing at ∼5 tons using a hydraulic press. To avoid thickness effects (i.e., self-absorption),[14] pellets were formed with a thickness (d) of 0.5 mm, satisfying the condition that $\Delta\mu x \leq 0.1$, where x is the effective sample thickness (d/cos45°) and $\Delta\mu$ is the absorption coefficient edge step at both the Pt L$_3$ and Ru K absorption edges. The wafer was then loaded into a custom designed and built catalyst cell which allowed simultaneous in situ X-ray fluorescence and transmission measurements over an operating temperature range of 150 to 773 K.

The in situ cell was purged with H$_2$ for 1 h after loading the sample wafer. The metered flow of H$_2$ (Matheson, 99.999%) was passed through sorbant traps (Alltech) to remove O$_2$ and water. The temperature was monitored with an Omega Chromel/Alumel thermocouple mounted directly on the sample mounting stage. The sample was activated by heating at a rate of 15 K/min in flowing H$_2$ (40 mL/min) to a cell-limited temperature of 673 K and held at that limit for 1 h. During the activation, the XANES region of the Pt L$_3$-edge was scanned. The samples were then cooled under H$_2$ to 190 K before making the EXAFS measurements. In addition, two intermediate temperatures were utilized. For these latter samples, the temperature was raised to either 423 or 473 K for 1 min. Both samples were then cooled rapidly (using liquid nitrogen), and the EXAFS data were measured at 190 K. X-ray absorption data for the Pt L$_3$- and Ru K-edges were also measured from the following reference metals as described elsewhere: Ru powder (Aldrich) and Pt foil (Aldrich).[11]

All X-ray absorption data were measured using the UIUC/Lucent Technologies beamline X16C at the National Synchrotron Light Source, located at the Brookhaven National Laboratory in Upton, NY. This beamline uses a sagitally focusing double-crystal monochromator with Si(111) crystals which focus the light to a 0.3 mm × 0.5 mm beam spot at the sample. The intensity of the focused beam (I_0) was measured with a 15-cm-long ion chamber filled with a 10:1 mixture of He/Ar. X-ray absorption data from the sample and the reference metals were measured simultaneously in fluorescence and transmission modes by scanning from 200 eV below to 1000 eV above the Pt L$_3$- and Ru K-edges. This was accomplished by turning the sample to ∼45° with respect to the beam direction and measuring the intensity of the transmitted (I_1) X-rays and the intensity of the X-ray fluorescence (I_f) from the sample. A 30-cm-long Ar-filled ion chamber placed after the sample (collinear with the beam direction) was used to measure I_1,

(12) Adams, R. D.; Wu, W. *Organometallics* **1993**, *12*, 1248.

(13) Urbancic, M. A. Ph.D. Thesis, University of Illinois at Urbana−Champaign, 1984.

(14) Tan, Z.; Budnick, J. I.; Heald, S. M. *Rev. Sci. Instrum.* **1989**, *60*, 1021.

and a Lytle detector (EXAFS Co.) placed at 90° with respect to the beam direction was used to measure I_f. The 4-cm-long Lytle detector was filled with Ar and Xe for data collected on the Pt L_3- and Ru K-edges, respectively. Thin samples of Pt and Ru metals were used to calibrate the beam energy during each scan of the Pt L_3- and Ru K-edges, respectively. The calibration measurement was made with a third Ar-filled ion chamber (I_2) placed after I_1. The positions of the metal absorption edges (Pt, 11564 eV; Ru, 22117 eV) could then be determined by placing the metal standard between ion chambers I_1 and I_2 and measuring the total absorption in I_2 due to the metal standard.

EXAFS Data Analysis. The analytical procedures used follow those described in detail elsewhere.[11] A summary is given here. The Pt L_3- and Ru K-edge EXAFS data were analyzed using the UWXAFS analysis package,[15] which determined structural parameters by fitting a theoretical EXAFS signal to the data. The data analysis was performed in the following order.

First, a smooth atomic background function, $\mu_0(E)$, was removed from the raw absorption coefficient, $\mu(E)$, using the AUTOBK method,[16] and the normalized EXAFS signal

$$\chi(k) = \frac{\mu(k) - \mu_0(k)}{\Delta\mu_0(0)} \qquad (1)$$

obtained. Here, the photoelectron wavenumber $k = (2m(E - E_0)/\hbar^2)^{1/2}$, where m is the electron mass, E is the X-ray photon energy, E_0 is the absorption edge energy, and $\Delta\mu_0(0)$ is an absorption edge jump. For the purpose of background removal, the energy reference E_0 was taken at the middle of the edge jump.

The resultant EXAFS signal is a sum of photoelectron paths: $\chi(k) = \sum_i \chi_i(k)$. The contribution of each path can be expressed in the form

$$\chi_i(k) = \frac{S_0^2 N_i}{kR_i^2} f_i(k)\, e^{-2k^2\sigma_i^2} \sin(2kR_i + \delta_i(k)) \qquad (2)$$

where S_0^2 is the passive electron reduction factor,[17] N is the coordination number of the shells of neighboring atoms, R is half the total scattering path length (or interatomic distance, in the case of the single-scattering paths), σ^2 is the relative mean square deviation (RMSD) of the distance (or XAFS Debye–Waller factor), and $f(k)$ and $\delta(k)$ are the effective scattering amplitude and phase shift, respectively. The computer code FEFF6[18] was used to calculate $f(k)$ and $\delta(k)$ for each path to the nearest shell of each absorbing atom, namely, Pt–Pt and Pt–Ru paths for the Pt central atom and Ru–Ru and Ru–Pt paths for the Ru central atom. The lattice parameter $a = 3.78$ Å was chosen for the reference fcc structure used in the FEFF6 calculations. Previous studies have conclusively shown that the final PtRu$_5$ nanoparticle adopts an fcc closest-packed structure.[11] Values of $S_0^2 = 0.81 \pm 0.04$ for the Ru K-edge and 0.81 ± 0.06 for the Pt L_3-edge data were obtained from analyses of the reference Ru powder and Pt foil, respectively.

The theoretical and measured EXAFS signals, $\chi(k)$, were multiplied by k^3 and then Fourier transformed into r-space where the nonlinear least-squares fits using eq 2 were performed by varying N, R, σ^2, and ΔE_0 (correction to the energy reference). We note, as has been pointed out by K. Pandya et al., that the bonding interactions of the metal centers with the support and the presence of other absorbed species on the nascent cluster complicates the analysis of the EXAFS data in terms of a temperature-dependent structural model for the carbon-supported Pt/Ru particles.[19] Because of the significant contributions from both metal and nonmetal (low-Z) neighbors in the Pt and Ru data measured

from the samples treated at 423 K, special care was taken to separately analyze each of these interactions. In this procedure, the residuals of the fit to the metal contribution were separately fit to approximate the low-Z contribution. A similar procedure was critically tested by Frenkel et al. in their structural analysis of the ferroelectric perovskite KNbO$_3$ where it was found possible to separately quantify the contributions of Nb–Nb (less disordered) and Nb–O (more disordered) interactions which contributed to the same r-range but had different effective k-ranges.[20]

In the first part of the procedure, the first-shell M–M interactions were simultaneously fit to the Pt L_3- and Ru K-edge data over a k-range of 3.5–13 Å^{-1} (r-range of 1.7–3.0 Å) using a k^3-weighting, similar to a procedure previously described.[11] The k^3-weighting factor was chosen to better separate metal from the low-Z neighbors which partially contribute amplitude to the same k-range. The lower limit of the k-range was chosen to be relatively large (3.5 Å) in order to minimize the contributions of the nearly collinear metal–CO configurations in the same distance as the metal–metal interactions. The heterometallic (R_{PtRu} and R_{RuPt}) bond distances and DWFs for this shell were constrained to be equal. The heterometallic coordination numbers were constrained so that

$$N_{Pt-Ru} = \frac{X_{Ru}}{X_{Pt}} N_{Ru-Pt} \qquad (3)$$

where X_M is the atomic percent composition of metal, M, in the nanoparticles ($X_{Ru}/X_{Pt} = 5$).[21] The uncertainties in the results obtained for the heterometallic bonds which contribute to the data sets were generally smaller than those found for the homometallic bonds.

The residuals of the first-shell metal were then analyzed for the Pt L_3- and Ru K-edge data to determine the structural parameters of the low-Z neighbors (found in the r-range of 1.1–1.7 Å). Because the difference between the M–O and M–C interactions is negligible with respect to the EXAFS signal, we modeled both of these interactions as M–O (where O represents a general low-Z backscatterer). FEFF6 was used to calculate Ru–O and Pt–O EXAFS signals (i.e., $f(k)$, $\delta(k)$) for model RuO$_2$ and PtO$_2$ structures, respectively. The reliability of the calculations was tested by fitting these parameters to the experimentally measured data for RuO$_2$ and PtO$_2$ powder samples. The Ru K-edge residuals were fit with FEFF6 theory for the Ru–O interactions with a k-range of 2–11 Å^{-1} and an r-range of 1.1–1.7 Å using the k^2-weighting. The fitting variables were the Ru–O coordination number N, correction to the model distance ΔR, mean-squared disorder σ^2, and ΔE_0. It is important to note that, in addition to correcting the FEFF6 theory for not taking into account the ionic contributions made to the character of the Ru–O bond, the ΔE_0 correction also compensates for the nontransferability of phase between the RuO$_2$ reference and the nanocluster data.[17] A similar procedure was performed to extract Pt–O (Pt–C) contributions from the Pt L_3-edge data.[22]

Results

The data which follow help establish the nature of the nucleation and growth processes which lead to the formation of carbon-supported PtRu$_5$ nanoparticles from the molecular carbonyl cluster precursor, PtRu$_5$C(CO)$_{16}$. The structure of these final metallic clusters has been characterized rigorously by EXAFS, ultrahigh-resolution transmission electron micros-

(15) Stern, E. A.; Newville, M.; Ravel, B.; Yacoby, Y.; Haskel, D. *Physica B* **1995**, *208 & 209*, 117. The UWXAFS package is licensed through the University of Washington.

(16) Newville, M.; Livins, P.; Yacoby, Y.; Rehr, J. J.; Stern, E. A. *Phys. Rev. B* **1993**, *47*, 14126.

(17) (a) Stern, E. A.; Heald, S. M. In *Handbook on Synchrotron Radiation*; Koch, E. E., Ed.; North-Holland: Amsterdam, 1983; Vol. 1, Chapter 10. (b) Koningsberger, D. C., Prins, R., Eds. *X-ray Absorption: Principles, Applications, Techniques of EXAFS, SEXAFS, and XANES*; Wiley: New York, 1988.

(18) Zabinski, S. I.; Rehr, J. J.; Ankudinov, A.; Albers, R. C.; Eller, M. J. *Phys. Rev. B* **1995**, *52*, 2995.

(19) Pandya, K. I.; Anderson, E. B.; Sayers, D. E.; O'Grady, W. E. *J. Phys. IV* **1997**, *7*, C2–955.

(20) Frenkel, A. I.; Wang, F. M.; Kelly, S.; Ingalls, R.; Haskel, D.; Stern, E. A.; Yacoby, Y. *Phys. Rev. B* **1997**, *56*, 10869.

(21) Via, G. H.; Drake, K. F.; Meitzner, G.; Lytle, F. W.; Sinfelt, J. H. *Catal. Lett.* **1990**, *5*, 25.

(22) We believe that separately fitting the metal and low-Z contributions was justified because the functional forms of the photoelectron backscattering amplitudes, $f(k)$, for these two types of scatterers are different. Specifically, the EXAFS scattering amplitude, $f(k)$, for low-Z scatterers is largest at values of k that are significantly lower than that for the metal scatterers. Thus, these two components were better separated by emphasizing the high k-range in the fit to the metal contribution and the low k-range in the fit to the low-Z contribution.

copy, electron microdiffraction, and electron-stimulated disper- sive X-ray analysis (EDX). These results have been described in detail in an earlier report[11] but are summarized here for the benefit of the reader. First, the heating of carbon-supported $PtRu_5C(CO)_{16}$ in a H_2 atmosphere leads to the formation of bimetallic nanoparticles (at the loadings used in the present work, the particles formed have an average diameter of $\sim$1.5 nm). The distribution of particle sizes is very narrow. More importantly, the distribution of the particle composition is sharply peaked on the 1:5 stoichiometry of the $PtRu_5C(CO)_{16}$ precursor, and no evidence was found which suggests segrega- tion of the Pt and Ru into separate particles. Preferential surface segregation of the Pt within the bimetallic nanoparticle is clearly indicated, however. These $PtRu_5$ clusters adopt a face-centered cubic closest-packed structure, an intriguing result given that, in bulk, alloys of this composition adopt an hcp structure. Taken together, the data show that the reductive condensation of the molecular precursors yields a well-defined population of bimetallic nanoparticles. The reactions involved are highly activated, requiring as they do the extrusion of the carbide core of the $PtRu_5C(CO)_{16}$ cluster and the loss of the coordinating carbonyl ligands. The temperature-dependent evolution of the system toward the firmly established closest-packed metallic structure is examined immediately below.

XANES Results. XANES data obtained for the Pt L_3-edge are shown in Figure 1. These data, measured at different tem- peratures during the reduction process and thus at different stages during the nucleation and growth of the $PtRu_5$ clusters, were carefully aligned in energy relative to the inflection point on the absorption edge jump of the reference metal (Pt foil) measured simultaneously with the $[PtRu_5]/C$ data, as described above. The shift between different data sets was defined as the energy difference between the data and the Pt reference in- flection points on the edge jump. Choosing Pt metal as a reference has an advantage because the defined shift naturally characterizes the transformation to the final metallic state of the particles (Figure 1b). The data clearly demonstrate that the edge energy progressively shifts during the heating cycle to a limiting value consistent with a metallic state.

TPRS Results. The results of the temperature-programmed reaction spectroscopy (TPRS) studies are summarized in the data presented in Figure 2. These data demonstrate that CO is lost from the cluster across a broad temperature range ($\sim$400– 600 K). The reaction onset lies below the lowest temperature for which an EXAFS data set was obtained. At the scale shown in the figure, gases evolved from the support contribute essen- tially zero intensity in either the $m/e = 15$ or 28 data channels. We were unable to detect a persuasive signal that could be assigned with certainty to the extrusion of the carbide core of the precursor cluster as methane (representative data shown for $m/e = 15$).

EXAFS Results. The Fourier transform (FT) magnitudes of the Pt L_3- and Ru K-edge EXAFS data, measured after treating the carbon-supported cluster precursor at various temperatures in H_2, and fits using FEFF6 theory are displayed in Figure 3. To better visualize the contributions of both the metal–metal and metal–low-Z interactions, the data was Fourier transformed using a large k-range ($2 < k < 13$ Å^{-1}) with k^3- weighting. Fits to the low-Z contributions to EXAFS for both Pt and Ru central atoms, as well as separate contributions of different paths (Pt–Pt, Pt–Ru, Ru–Pt, and Ru–Ru) to the total signal in r-space, are given in the Supporting Information. Quantitative structural information about the Pt and Ru coor- dination environments (i.e., bond distances, R; coordination
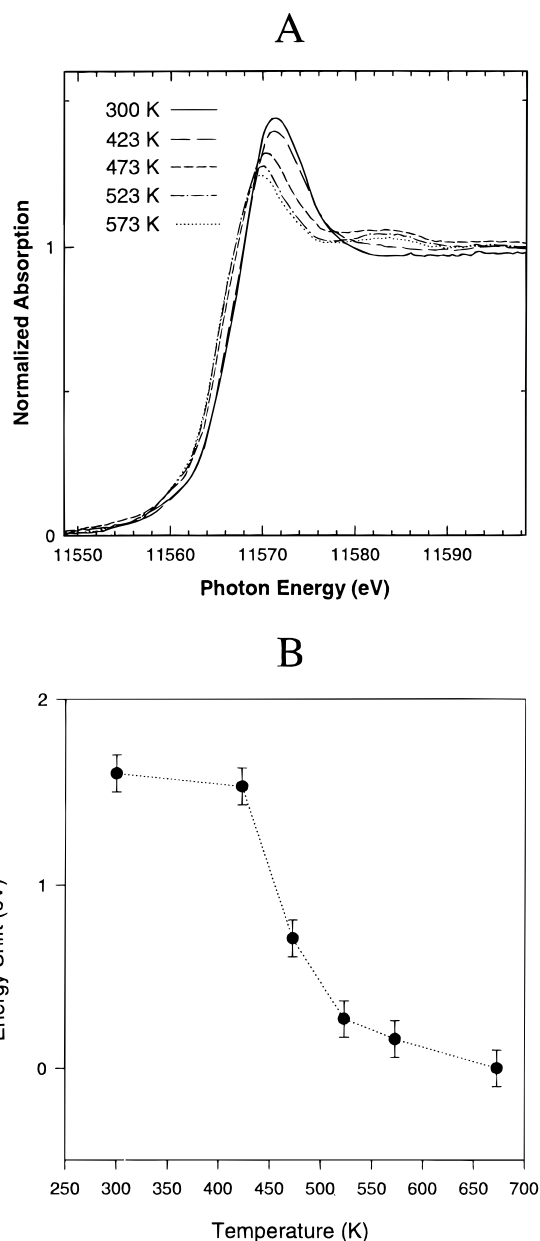
Figure 1. (A) Comparison of the Pt L_3 normalized near-edge X-ray absorption spectra during the activation of the carbon-supported $PtRu_5C$-$(CO)_{16}$ molecular cluster precursor under H_2 (1 atm). (B) Shift (relative to the Pt metal foil) of the binding energy in the Pt–Ru nanoparticles during their evolution to the metallic state.

numbers, N; and the mean square deviation in R, σ^2) as well as ΔE_0 corrections to the energy origin were extracted from each spectrum using the fitting procedures described above. These results are summarized in Table 1 and graphically displayed in Figure 4. The coordination numbers for the metal–low-Z interactions found at reduction temperatures above 423 K are smaller than their uncertainties and thus statistically indistin- guishable from a net value of zero. The trends clearly evidenced in these data suggest that heating leads to a progressive evolution of the Pt–Pt, Pt–Ru, and Ru–Ru bonding interactions within the increasingly metallic ensembles.

STEM Results. Representative darkfield electron micro- graphs showing a collection of >250 nanoparticles after treating in H_2 at 473 K for 1 min and 573 K for 1 h are shown in Figures 5A and 5B, respectively. The results of a detailed STEM study have been reported previously.[11] Of interest in the current context is the qualitative illustration afforded by the images that
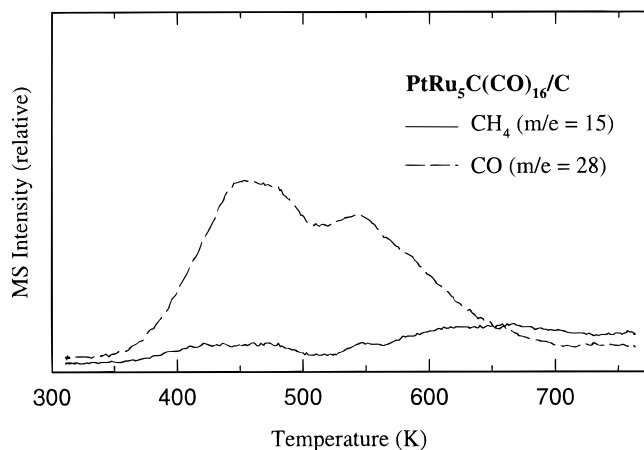
Figure 2. Temperature-programmed reaction spectra for the thermal decomposition of carbon-supported $PtRu_5C(CO)_{16}$ in H_2 recorded at values of m/e diagnostic for the evolution of CO ($m/e = 28$) and methane ($m/e = 15$).

the heating leads to the growth of larger and increasingly more coherent particles across the temperature range.

Discussion

The structure of the cluster precursor used in this study consists of an octahedral metal framework that encapsulates a stabilizing carbide core (Scheme 1). Each metal (bearing a complement of coordinating carbon monoxide ligands) has four metal nearest neighbors with an average bond distance of 2.9 Å.[23] Dispersing the cluster precursor on a carbon support and heating under a H_2 atmosphere leads to the formation of nanometer-sized alloy particles with an average M−M bond distance of 2.67 Å, hereafter referred to as [$PtRu_5$]/C. We have shown previously that these nanoparticles exhibit a Pt:Ru composition of 1:5 and an exceptionally narrow size distribution centered on ca. 1.5 nm and adopt an approximately hemispherical, face-centered cubic (fcc) closest-packed structure.[11] The average [$PtRu_5$]/C nanoparticle results from the reductive condensation of ∼6 precursor molecules and thus contains ∼36 atoms.

Heating the carbon-supported precursor molecules in H_2 results in the loss of the carbon monoxide ligand shell as evidenced by mass spectral analysis of the product effluent. The desorption of carbon monoxide must occur via an exchange with bonds to hydrogen, the carbon support, or more metal atoms. Further insights into the nature of this process were obtained by examining the X-ray absorption near-edge structure of the Pt L_3-edge during the reduction process (Figure 1). The absorption-threshold resonance observed at the Pt L_3-edge results from the excitation of $2p_{3/2}$ core level electrons into unoccupied 5d states.[24,25] The resonance intensity, which is strongly correlated with the density of states (and thus oxidation state and electronic structure) of the absorbing Pt atoms, displays a dramatic reduction in amplitude during the temperature ramp

to 673 K. The data also show that the thermal treatment results in a shift in the edge position to lower binding energies. Most of the changes seen by XANES occur in the temperature range of 423−473 K. The data suggest that the disruption of the cluster framework above 423 K leads to the loss of the CO ligands with a likely substitution of metal−metal (and perhaps metal−hydrogen) bonds.

The larger value of the Pt $2p_{3/2}$ binding energy (BE) and more intense white-line found at temperatures below 423 K are consistent with the presence of a significant fraction of the Pt bound in the form of $M_x(CO)_y$ surface complexes. Such an interpretation is supported by X-ray photoemission and X-ray absorption studies of supported carbonyl clusters. For example, X-ray photoemission studies of $[Pt(CO)_3]_n^{2-}$ molecular clusters indicate that the core-level 4d and 4f binding energies are consistently 2 eV higher than the value found for bulk Pt metal.[26] Our XANES results are in good agreement with this finding (Figure 1b). The Ir $4f_{7/2}$ BE measured for silica-supported $Ir_4(CO)_{12}$ clusters was ca. 3 eV greater than the bulk Ir metal value.[27] Such effects are due to the acceptor properties of the CO ligands (which reduce the electron density on the metal) and differences in the extra-atomic relaxation (i.e., final state effects) as compared with that of the bulk metal. The larger white-line intensity is also consistent with charge donation from the Pt to the CO ligands (or the support). We note that it has been proposed that an increase in the white-line intensity also would result if the size of a metallic nanoscale ensemble decreased as well.[28]

The loss of the stabilizing CO shell from the cluster precursor in the presence of hydrogen results in the formation of an increasingly metallic state. Examination of the cluster activation process in a H_2 atmosphere by TPRS revealed that CO is evolved from the sample (along with a quantity of methane) across a very broad temperature range (from 350 to 550 K). The TPRS data presented in Figure 2 show that the maximum in the CO desorption rate occurs near 450 K, a temperature where the EXAFS data discussed below suggest that significant changes occur in the nascent alloy cluster nanostructure. Very little of the carbon content of the cluster is converted to methane under these conditions. Taken together, the TPRS data strongly suggest that some quantity of the metal species involved in the nucleation and growth process below 500 K are metal−carbonyl complexes.

To further probe these temperature-dependent structural changes, the local coordination environment of each metal atom was probed using EXAFS spectroscopy.[17] The utility of this technique stems from the ability of EXAFS to probe the local bonding environment present around both the Pt and Ru centers (even without the occurrence of long-ranged order). This feature makes EXAFS an ideal method to study heterometallic nanophase materials since the structural order present in a nanometer-sized ensemble is of the order of the length scale probed by the spectroscopy. In addition, the element specificity provides a measure of the relative ordering exhibited by the two metals present in the alloy nanoparticle.

The FT of the k^3-weighted EXAFS data (Figure 3) provides a convenient representation of the qualitative changes occurring in the average coordination environment of the absorbing Pt and Ru centers during the nanoparticle condensation process.

(23) Adams, R. D.; Wu, W. *Organometallics* **1993**, *12*, 1248. The M−M bond distances ranged from 3.05 to 2.78 Å in the metal−carbonyl cluster.

(24) (a) Lytle, F. W. *J. Catal.* **1976**, *43*, 376. (b) Mansour, A. N.; Cook, J. W.; Sayers, D. E. *J. Phys. Chem.* **1984**, *88*, 2330. (c) Meitzner, G.; Via, G. H.; Lytle, F. W.; Sinfelt, J. H. *J. Phys. Chem.* **1992**, *96*, 496.

(25) The resonance intensity is affected by changes in the oxidation state of the absorber; however, more subtle effects such as dispersion or changes in the interaction with the support are also important. The edge position, which is in large part related to the binding energy of the Pt $2p_{3/2}$ electrons, will be affected by changes in the valence electronic structure and changes in the extra-atomic relaxation (i.e., final state effects) [Citrin, P. H.; Wertheim, G. K. *Phys. Rev. B.* **1983**, *27*, 317].

(26) Apai, G.; Lee, S.-T.; Mason, M. G.; Gerenser, L. J.; Gardner, S. A. *J. Am. Chem. Soc.* **1979**, *101*, 6880.

(27) Comelli, G.; Sastry, M.; Paolucci, G.; Prince, K. C.; Olivi, L. *Phys. Rev. B.* **1991**, *43*, 14385.

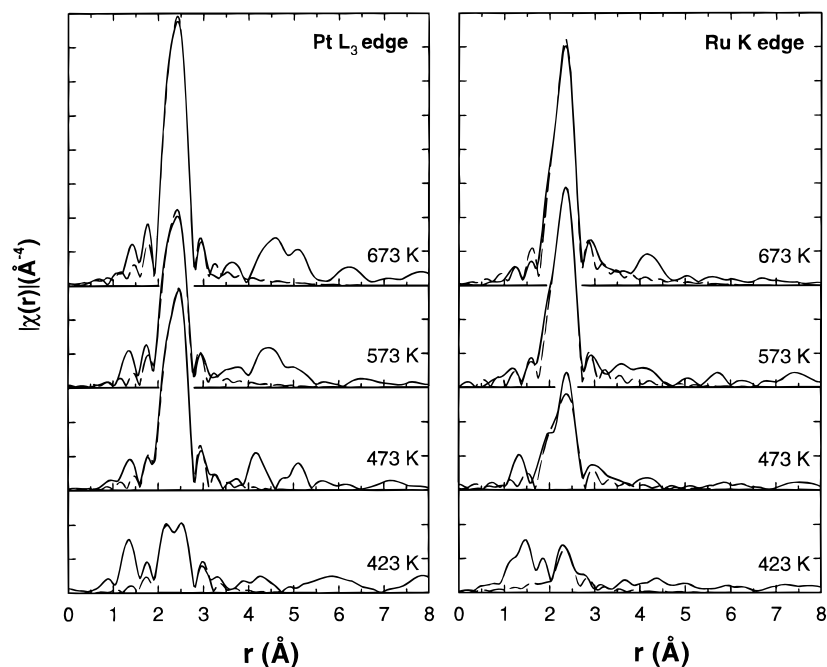(28) Bazin, D.; Sayers, D.; Rehr, J. J.; Moffet, C. J. *Physics (Long Island City, N.Y.)*, in press.

Figure 3. Fourier-transformed (A) Pt L_3-edge and (B) Ru K-edge EXAFS data (k^3-weighted) measured at 190 K from the carbon-supported [PtRu$_5$] nanoparticles after activation under H$_2$ at (a) 423 K (1 min), (b) 473 K (1 min), (c) 573 K (1 h), and (d) 673 K (1 h). Dashed lines indicate the first-shell fit to the metal contribution (*r*-range, 1.7−3.0 Å).

Table 1. First-Shell Structural Parameters Determined by Fitting the Metal and Low-Z Portions of the Pt L_3- and Ru K-Edge EXAFS Data Measured during the Reductive Condensation of Carbon-Supported [PtRu$_5$] Nanoparticles in a H$_2$ Atmosphere

temp (K)		Pt first shell			Ru first shell		
		Pt−low-Z^a	Pt−Pt	Pt−Ru	Ru−low-Z^a	Ru−Pt	Ru−Ru
673	N		2.1(7)	4.4(1.4)		0.9(3)	5.9(6)
	R (Å)		2.724(3)	2.71(1)		2.71(1)	2.673(4)
	σ^2(Å^2)		0.0024(15)	0.0040(18)		0.0040(18)	0.0050(5)
	ΔE_0		5.3(5)	5.3(5)		−2.7(1.1)	−2.7(1.1)
573	N		2.8(1.0)	4.2(1.1)		0.8(3)	5.4(6)
	R (Å)		2.71(1)	2.70(1)		2.70(1)	2.669(4)
	σ^2(Å^2)		0.0080(18)	0.0047(16)		0.0047(16)	0.0057(6)
	ΔE_0		2.2(6)	2.2(6)		−0.7(1.2)	−0.7(1.2)
473	N		3.4(1.1)	5.5(9)		1.1(2)	2.8(2)
	R (Å)		2.744(8)	2.711(7)		2.711(7)	2.683(2)
	σ^2(Å^2)		0.0096(17)	0.0055(7)		0.0055(7)	0.0049(4)
	ΔE_0		4.6(4)	4.6(4)		−0.1(8)	−0.1(8)
423	N	1.2(0.1)	3.8(1.3)	2.7(7)	1.5(3)	0.5(2)	3.9(2.5)
	R (Å)	1.89(1)	2.80(2)	2.74(1)	1.87(2)	2.74(1)	2.63(2)
	σ^2(Å^2)	0.0126(11)	0.0093(28)	0.0058(13)	0.0044(26)	0.0058(13)	0.0141(47)
	ΔE_0	2.9(7)	5.7(1.5)	5.7(1.5)	0.0(2.8)	0.0(2.6)	0.0(2.6)

^{a} Modeled as an M−O scattering interaction. This analysis does not distinguish between M−O and M−C scatterers, although the latter interaction is believed to be the more important.

Inspection of the data for both edges shows that the intensity of the peak centered between 2 and 3 Å, resulting from Ru−M and Pt−M bonding interactions,[11] generally increases with the annealing temperature. In addition to the metal contribution, the Pt and Ru data also show significant structure below 1.5 Å in spectra measured below 423 K (although these contributions decline dramatically above this temperature). These latter low-*r* peaks result from interactions occurring between the metals and low-Z elements (i.e., C). This conclusion was confirmed by analyzing this region using suitable models for these bonding interactions (i.e., PtO$_2$ and RuO$_2$). Previous studies by EXAFS of homometallic Pt clusters[29] provided similar results for the temperature-dependent evolution of Pt−low-Z coordination numbers and the interatomic distances as found in our work (Table 1).

(29) Shido, T.; Yamamoto, T.; Harada, M.; Ichikawa, M. *J. Phys. IV.* **1997**, *7*, C2−855.

The distribution of metal structures formed after heating the molecular precursors to 423 K in H$_2$ includes metal−carbonyl species and incipient metal nanoparticles. Three pieces of evidence from the EXAFS data support this conclusion. First, the fragmentation of the precursor metal framework was implied by the lack of metal neighbors at a distance of 2.9 Å in either the Pt or Ru edge EXAFS data (Figure 4). Instead, these interactions are replaced by metal nearest neighbors at shorter bond distances (i.e., 2.6−2.8 Å). The shorter metal bond distances reflect nucleation of metal aggregates with a structure that is more consistent with the final close-packed nanoparticle than that of the cluster precursor.[11] The significant difference between the metal bonding seen in this intermediate state and that found in the final nanoparticle structure is the large static disorder (i.e., large σ^2 for the metal bonds) and the presence of 1−2 M−CO bonds. In fact, the large degree of static disorder is likely a direct result of the continued bonding of CO ligands

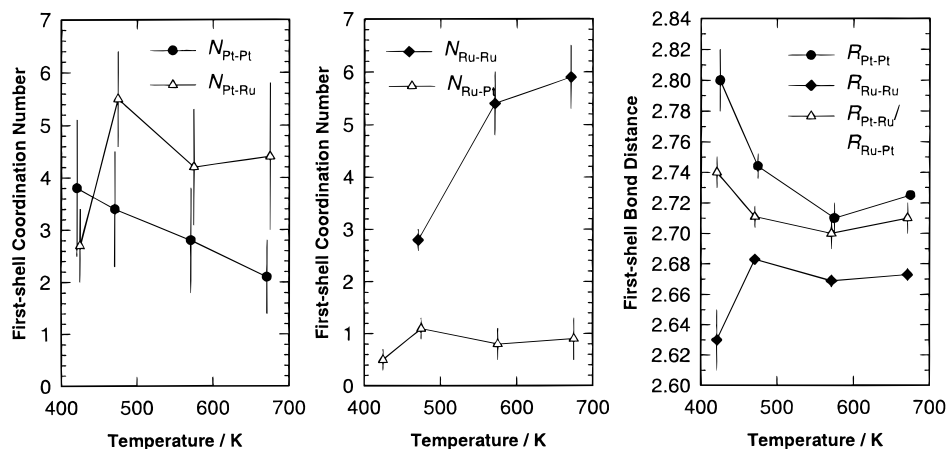**Figure 4.** Evolution of the first-shell coordination environment during reduction in H_2. The Pt (N_{Pt-Pt} and N_{Pt-Ru}) and Ru (N_{Ru-Pt} and N_{Ru-Ru}) coordination numbers are shown in (A) and (B), respectively. The Pt (R_{Pt-Pt} and R_{Pt-Ru}) and Ru (R_{Ru-Pt} and R_{Ru-Ru}) bond distances are shown in (C). The EXAFS amplitude is too low to reliably determine a Ru first-shell coordination number at 423 K.

which must act to alter the bond distances and coordination numbers from the ideal close-packed geometry.[30]

A closer examination of the metal shell structure around the Pt and Ru atoms provides further evidence as to the nature of the incipient nanoparticle structure formed at 423 K. Specifically, the presence of a substitutional Pt−Pt bonding contribution indicates that the average metal ensemble includes metal atoms from separate cluster precursors. We note that the average coordination structure of the metal atoms associated with the nanoparticles also suggests that the complete coalescence of all the metal atoms of the precursor has not occurred, however. This is illustrated most dramatically by the large differences seen in the Pt and Ru homometallic bond distances (see Table 1 and Figure 3), which may reflect the incomplete alloying of the two metals. Again, these results support the finding that a significant fraction of the CO bonding which remains must disrupt the complete alloying of the two metals. As we show below, the order of the incipient particles increases dramatically upon heating to 473 K.

The most significant change occurring over the temperature range 423−473 K is the increase seen in the fraction of Ru associated with an ordered nanoparticle domain. The increasing "coalesced" fraction of Ru in the nanoparticles is exhibited by the Pt and Ru metal coordination numbers and the bonds distances found for Pt and Ru after heating to 473 K. Specifically, the decrease in the Ru−low-Z coordination number is correlated with an increase in the Ru−M bonding and also accompanied by a significant decrease in the static disorder (σ^2) found in the Ru−Ru shell. In contrast, the Pt data indicated that the Pt−Pt coordination number and order did not change even though the Pt−Ru coordination numbers increased significantly. The increase in the M−Ru coordination was also reflected in the changes seen in the average bond distances separating the metals, which all converge toward the value found in the final particle structure. The decrease in the measured M−Pt bond distances toward the value found in the final nanoparticles is also consistent with an increased degree of alloying.

Although the EXAFS data clearly demonstrate the increase in the fraction of Ru associated with the incipient nanoparticles, we note that the distribution of metal atoms is significantly different from that found in the final structure. Specifically, we find that the number of Pt−Ru and Pt−Pt bonds results in a significantly larger Pt−M coordination (8.9 ± 2.0) than the Ru−M coordination (3.9 ± 0.4). These coordination numbers suggest an incomplete coalescence of the Ru into the ordered nanoparticle structure.

The significant change in the structure of the nanoparticles found after heating the system to temperatures >573 K largely centered on a significant increase in the measured Ru−Ru coordination numbers. We believe that this occurs as Ru, which may be present as fragments of the precursor, continues to nucleate on the growing particles. The increase in the number of Ru−Ru bonds is not accompanied by a significant change in the number of Pt−Ru or Pt−Pt bonds at this temperature, however. Thus, to within experimental certainty, the Pt−M coordination environment shows only modest changes which result in the net equalization of the Pt−M and Ru−M coordination numbers (6.5 ± 2.1 and 6.8 ± 0.9, respectively).

The interpretation of the average structural changes which occur during the nanoparticle growth is based on a comparison between the coordination numbers and the size of the nanoparticles. As described in our earlier report, the average metal coordination numbers may be used to estimate the average nanoparticle diameter using as a model a fcc hemispherical cuboctahedron.[11,31] The coordination numbers measured here for low-temperature treatments in H_2 ($T \leq 473$ K) suggested that the average sizes of the nanoparticles do not exceed ca. 8 Å. These data correlate closely with electron microscopy data measured for 250 nanoparticles which revealed nanoparticles with an average diameter of 9 Å and 1σ of 2 Å (Figure 5A). The sizes measured continue to increase with the thermal treatment, and ultimately, the species formed comprise particles with an average diameter of ca. 15 Å (Figure 5B).

One aspect of the high-temperature structural evolution that is most striking is the change which occurs in the relative number of metal neighbors bound around the Pt and Ru centers (Figure 3). After being heated to 473 K, EXAFS reveals that the Pt atoms have a significantly larger first-shell metal coordination number than does Ru. This suggests that, during this treatment, the Ru binds to Pt centers which had previously

(30) Mass-balance principles also suggest that contributions of the M−CO complexes to the EXAFS are negligible for the data taken above 423 K for several reasons. First, these interactions are highly disordered and thus contribute little amplitude. Second, the isothermal heating procedure used progressively and substantially depletes these states (relative to the M−M bonded fractions) and, thus, renders the analysis insensitive (above 423 K) to their presence (except for the possible effects they have on the relative disorder seen in homometallic and heterometallic bonding interactions)

(31) The weighted average coordination was calculated using the following relation: $N_{M-M} = (N_{Pt-M} + 5N_{Ru-M})/6$.
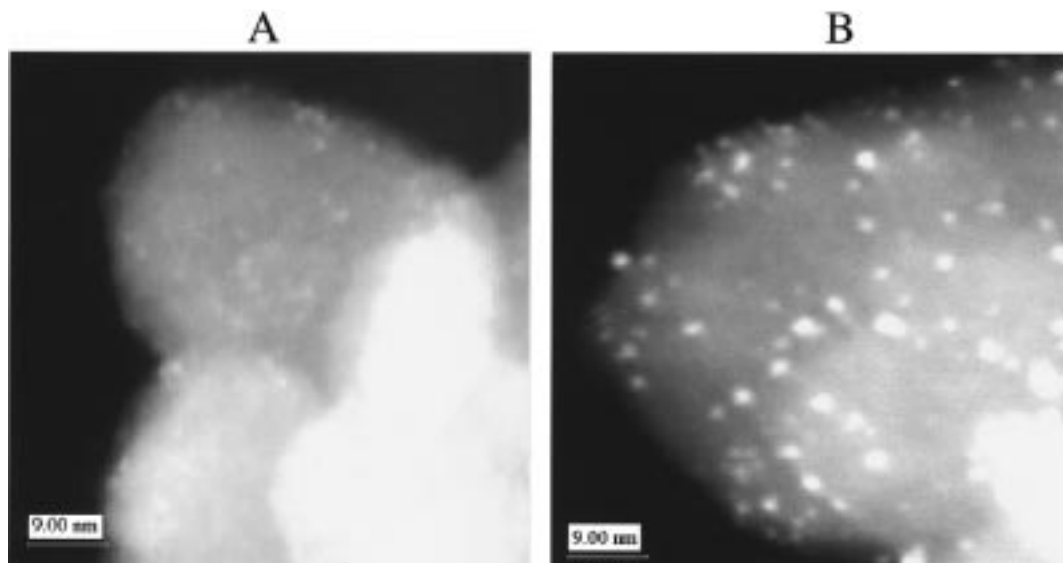
Figure 5. Representative STEM dark field images ($\times 10^6$, 100 kV) of the carbon-supported [PtRu$_5$] nanoparticles after treatment in H$_2$ at (A) 473 K (1 min) and (B) 573 K (1 h).

coalesced to form a core structure at the center of the nanoparticle (Scheme 1). Interestingly, as the size of the nanoparticles increases during the heat treatment, the Pt coordination abruptly begins to trend toward lower values. More important, though, we find that the first-shell coordination numbers for the two metals (which are now roughly equal, Figure 3) suggest a nonstatistical distribution of the Pt and Ru atoms in the binary nanoparticle. These significant changes likely result from the restructuring of the particles upon annealing in H$_2$ at the higher temperature. This final nanoparticle structure, which has been described in detail elsewhere (one which follows from the multiple-shell fit of the EXAFS data which accounts for the dominant multiple-scattering interactions), exhibits a preferential segregation of Pt toward the surface of the nanoparticles and a pronounced preference for the formation of Pt−Pt over Pt−Ru bonds at this interface.[11] These aspects of the final nanoparticle structure are depicted qualitatively (albeit overly simplistically) in Scheme 1.

The redistribution of the Pt toward the surface of the nanoparticles must reflect the energetically favored structure for the bare (or hydrogen-covered) particles. Thus, the difference in the metal distribution for the low-temperature treatments must be related to the kinetics or the energetics of the system which in turn themselves are mediated by both ligands (such as CO) and adsorbates as well as the support interactions. We discuss each of these effects in turn and provide suitable comparisons to previously prepared molecular and supported metal clusters.

We believe the formation of a high coordination environment Pt core results from the kinetically controlled reductive nucleation of fragmented Ru species onto incipient Pt-rich nanoparticles. Such a mechanism for the growth process may provide a template for the nucleation of the final fcc nanoparticles, one which is different from the hexagonal close-packed (hcp) structure predicted by the bulk phase diagram.[32] Similar structural arguments regarding supported bimetallic nanoparticles have been described in the literature. For example, Pt−Re nanoparticles supported on silica were found to have an fcc structure.[33] It was suggested that the Re, which probably reduces at a higher temperature than the Pt, grows epitaxially

on a Pt core structure. The template mechanisms provide what is essentially a kinetic argument for rationalizing the phase behavior of a nanoscale system. It is therefore very important to note that, in the present system, the Pt core reconstructs with its constituent atoms ultimately segregating to the nanoparticle surface. The fcc close-packed structure of the [PtRu$_5$]/C nanoparticles is thus likely one which results from thermodynamic rather than kinetic control of the growth process. This provides clear evidence that the finite size of the nanoparticle, with its large fraction of surface atoms, is likely the major influence directing the growth habit. We also note that preferential surface segregation of one of the metal components may be promoted by differences in the bond energies between Pt and Ru to CO and/or hydrogen. Such adsorbate-induced segregation effects find precedent in the structures evidenced by molecular clusters and bimetallic colloids. Large molecular carbonyl clusters containing one metal component in the core have been synthesized and structurally characterized.[34,35] A notable example is provided by the [Pt$_4$Rh$_{18}$(CO)$_{35}$]$^{4-}$ carbonyl cluster in which a tetrahedral Pt core is encapsulated by an 18-atom Rh cage.[35] The formation of this structure has been related to the balance between the M−CO and M−M bond energies which, on going from the first to the third transition row, increasingly favors M−M bonding rather than M−CO interactions.[36] Similar structural rearrangements also have been demonstrated to occur in Pd−Cu colloids where reversible enrichment of Pd on the surface was found upon exposure of the colloid particles to CO. This process was concluded to be driven by the stronger Pd−CO bond as compared to that for Cu.[37]

Taken together, the data presented in this paper demonstrate that the fcc structure of the [PtRu$_5$]/C nanoparticles is obtained via thermodynamic control. The template effect seen in this system, the coalescence of Ru centers on a Pt-rich core, generates a transient structure which undergoes a further reconstruction to give the final 1.5-nm average diameter fcc nanoparticles.

(32) Okamoto, H. In *Binary Alloy Phase Diagrams*, 2nd ed.; Malaski, T. B., Okamoto, H., Subramanian, P. R., Kacprazate, L., Eds.; ASM: Materials Park, 1990; Vol. 3, p 2345.

(33) Liang, K. S.; Chien, F. Z.; Hughes, G. J.; Meitzner, G. D.; Sinfelt, J. H. *J. Phys. Chem.* **1991**, *95*, 9974.

(34) Ceriotti, A.; et al. *Angew. Chem., Int. Ed. Engl.* **1985**, *24*, 697.

(35) Fumagalli, A.; Martinengo, S.; Ciani, G.; Masciocchi, N.; Sironi, A. *Inorg. Chem.* **1992**, *31*, 336.

(36) Chini, P.; Longoni, G.; Albano, V. G. *Adv. Organomet. Chem.* **1976**, *14*, 311.

(37) Bradley, J. S.; Via, G. H.; Bonneviot, L.; Hill, E. W. *Chem. Mater.* **1996**, *8*, 1895.

These solid-phase materials thus display a rich phase behavior in which the normally subtle effects of surface energetics can come to play an extremely important (and in this instance, decisive) role.

Supporting Information Available: Supplementary data include plots of first-shell component fits to all the data presented in Table 1 (10 pages, print/PDF). See any current masthead page for ordering information and Web access instructions.

JA980638Z